Nanosecond MD of battery cathode materials with electron density description

de Blasio, Paolo Vincenzo Freiesleben; Jorgensen, Peter Bjørn; Lastra, Juan Maria Garcia; Bhowmik, Arghya

Published in:
Energy Storage Materials

Link to article, DOI:
10.1016/j.ensm.2023.103023

Publication date:
2023

Document Version
Publisher's PDF, also known as Version of record

Energy Storage Materials 63 (2023) 103023

Contents lists available at ScienceDirect

Energy Storage Materials

journal homepage: www.elsevier.com/locate/ensm

Nanosecond MD of battery cathode materials with electron density description

Paolo Vincenzo Freiesleben de Blasio [a], Peter Bjørn Jorgensen [b], Juan Maria Garcia Lastra [b], Arghya Bhowmik [*,b]

[a] Technical University of Denmark (DTU) Kongens Lyngby 2800 Denmark
[b] Technical University of Denmark (DTU), Technical University of Denmark Kongens Lyngby, 2800 Denmark

ARTICLE INFO

Keywords:
Machine learning
Graph neural network
Charge density prediction
Intercalation cathode
Ionic diffusion

ABSTRACT

Potentials derived with machine learning algorithms achieve the accuracy of high-fidelity quantum mechanical computations such as density functional theory (DFT), while allowing orders of magnitude lower computational time. In this work, we demonstrate the use of uncertainty aware equivariant graph neural networks for predicting spin-resolved electron densities, forces, and energies of the $Na_3V_2(PO_4)_3$ NASICON structured cathode. Due to the speedup in computational time, we are able to investigate structures of $\sim$300 atoms for 200 million timesteps. The ability to model larger systems on the nanosecond length scale with maintaining DFT level accuracy allowed critical insights into the diffusion characteristics of Na-ions, associated electron transfer processes, and dependence of diffusivity on sodium concentration in the structure.

1. Introduction

High accuracy electronic scale simulations with density functional theory (DFT), especially ab initio molecular dynamics (AIMD), have been a key to modelling electrochemical phenomena such as ionic diffusion that determine the functional properties of battery materials [1]. Discovering ionic diffusion mechanisms with high energy barrier (e.g. in intercalation battery cathodes) is very challenging. The time scale and system size required are often beyond what AIMD simulations allow due to computational cost. As those are coupled with electron transfer processes, classical force field methods lack the accuracy and electronic scale description of the electron transfer redox process at transition metal atoms of the intercalation framework while ions move through it. Over the last decade the promise of machine learning (ML) potentials has matured from conceptual development [2,3] to enabling long time and length scale simulations of real functional materials [4,5] with quantum mechanical accuracy but at much lower computational cost. High-accuracy long time-scale simulations with machine learning potentials recently have helped create new scientific insight in liquid hydrogen [6] and disordered silicon [7]. ML potentials have been applied in few cases for atomic-scale simulations of battery anode [8–10], electrolyte [11–15], cathode [16] and cathode coating materials [17] as well. These studies exemplify structural optimisation simulations of intercalated electrodes [8–10,16] and diffusion in solid state electrolytes [11–13,17] with ML potentials.

Simulations performed with ML potentials in these pioneering applications in battery materials do not encompass reactive diffusion, where electronic reorganisation, i.e. redox processes, happens. Compared to ML potentials that show good accuracy for structural optimisation calculations, building ML potentials for studying diffusion phenomena reliably is more challenging. For precise optimisation simulations, the surrogate models need to accurately represent only the near-equilibrium part of the potential energy surface (PES). High accuracy simulation of diffusive behaviour requires the surrogate to accurately portray a much larger portion of the PES, for bonding and electronic structure far beyond equilibrium covering transition state geometries and oxidation states [18,19]. If the underlying electronic structure does not change significantly, the degrees of freedom to be sampled and modelled in ML potentials are limited to structural ones and thus are less demanding than modelling diffusion in transition metal based frameworks (e.g. intercalation cathodes) where ionic diffusion also leads to redox reactions. The invariance of the electronic structure to the instantaneous position of diffusing ions and the limited modulation in the host lattice in solid state electrolytes[20,21] helps ML potentials with limited algorithmic expressivity perform well. Recent published work used ML potentials for ionic diffusion studies in systems

* Corresponding author.
E-mail address: arbh@dtu.dk (A. Bhowmik).

https://doi.org/10.1016/j.ensm.2023.103023
Received 26 February 2023; Received in revised form 1 September 2023; Accepted 18 October 2023
Available online 25 October 2023

where diffusive phenomena are not ion-coupled electron transfer [11,12,17]. Ionic diffusion coupled redox reactions in transition metal based cathode materials are expected to be exceptionally challenging due the combination of host framework structural modulation (with far from equilibrium structures during diffusion), electron transfer redox processes, and the presence of many atom types with multivalent transition metals. Currently published work on ML potentials for transition metal oxide intercalation cathode is built for optimisation tasks in the fully discharged state [16].

Due to the intricacy of building ML potentials that reliably model electron transfer based reactive/diffusive ML systems, such potentials have been successfully deployed only for small molecule reactions[18,19,22]. Gaussian approximate potential (GAP)[5] type of potential is applied in one of the studies [22]. GAP is not suitable for complex polyanionic cathodes with four or more types of atoms, as the number of 'smooth overlap of atomic positions' (SOAP) descriptors [5] needed increases combinatorially with the number of atom types. GAP potentials are difficult to train with a large number of training samples(cubic complexity to dataset size) which is needed to capture different 'away from equilibrium' structures that represent the diffusive system [19]. As the ML potentials development is data driven in nature, sampling the PES for higher energy configurations e.g. transition states need to sampled. Models built with mainly with near equilibrium structures would provide erroneous force and energy estimates for out of distribution structures encountered during simulations and thus not usable for reactive dynamics. Learning from our success in building generalised reactive ML potential for small molecule reactions [18,19], we obtained breakthrough in building reactive ML simulation tools that can perform electron density simulations similar to typical AIMD simulations.

We propose an equivarient graph neural network(GNN) based atomic scale simulation model that follows the state of the art development [23,24] in continuous filter GNNs with message passing based representation learning framework, enabling potentials capable of generalising for a large number of atomic species as required for complex polyanionic cathodes. We go beyond the state of the art by introducing an additional linear scaling equivariant GNN model for spin-resolved 3D electron density simulations. The model output is continuous and differentiable, but can be used to predict charge densities at grid points around atomic structures independent of each other, making it highly parallel and fast. This additional access to electron density while performing GNN based AIMD helps us to, for the first time, study the dynamic redox process occurring during ionic diffusion in intercalation cathode materials.

We used this equivariant GNN based machinery to study the electron transfer coupled diffusion mechanism in NASICON structured $Na_3V_2(PO_4)_3$, as this type of phosphate materials has attracted much attention as viable alternatives to lithium ion batteries [25,26] with good cycle life and energy density [27,28]. Specifically, recent studies have suggested the possibility of complex diffusion mechanisms based on vacancy and charge ordering [29]. We could simulate structures of $\sim$ 300 atoms for as much as 200 million timesteps. The ML models are able to capture complex diffusion mechanisms inside the structure.

2. Methods

2.1. Workflow

To gain a mechanistic understanding of the ionic mobility and

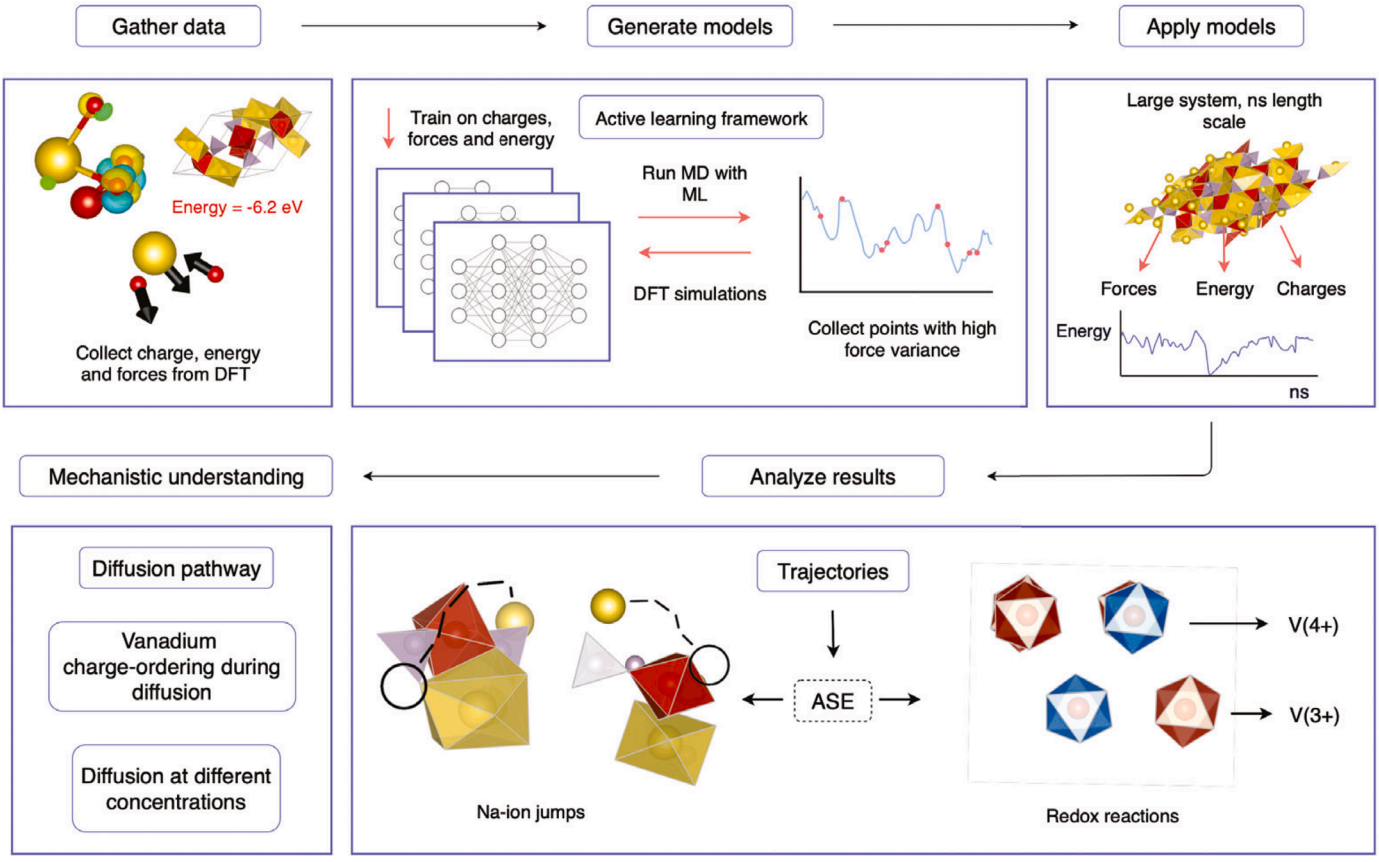

Fig. 1. Schematic of the ML workflow utilized in this article. In the first phase, we collect charges, forces and energies from DFT simulations. We then train an ensemble of ML models (to capture uncertainty) with energy, forces and charge density as target. Subsequently an active learning framework to iteratively retrain models with new out of distribution data for improving their accuracy and reliability. Finally the models are able to do nanosecond length scale MD, on a supercell of 300 atoms for our current study. We later analyze the results of the MD, at different charged state and temperatures.

related electron transfer mechanism in energy storage materials using ML, we developed a systematic workflow that can be applied to any crystalline material - anodes, cathodes or electrolytes. The diagram is illustrated in Fig. 1, and consists of the following steps:

1) Create initial datasets from short AIMD simulations starting with different intercalation state and ion ordering to get charge densities, forces and energies.

2) Train an ensemble (to get uncertainty estimates) of ML models (with energy, force, and charge density targets) on the initial dataset.

3) To improve the accuracy of the models and obtain reliable long-time scale MD, sample unknown parts of the configurational space using an active learning framework to retrain better models iteratively.

4) Apply models for molecular dynamics, charge prediction, or structure optimisation on long time (nanoseconds) and length scales (hundreds to thousands of atoms).

5) Analyse results and gain mechanistic understanding of the material.

2.2. Ab inito simulations

Spin polarized density functional theory based simulations were performed with the Vienna Ab-initio Simulation Package (VASP) [30]. The projector augmented wave (PAW) method [31] was used with a 400 *eV* energy cutoff. Exchange correlation effects were described using the PBE functional [32]. To improve the delocalisation error for d-electrons, a correcting Hubbard U term was added to the 3*d* electrons of the vanadium atoms. Following previous work, a $U-J$ parameter of 4.2 *eV* was added to vanadium atoms [33,34]. For the supercell with 2 formula units (f.u) $Na_3V_2(PO_4)_3$ (*NVP*), we use a k-point sampling of $2 \times 2 \times 2$, and for the 16 f.u. structure, we reduce the k-point sampling to $1 \times 1 \times 1$.

Ab initio molecular dynamics were run in the canonical NVT ensemble, using the atomic simulation environment (ASE) [35]. To increase the likelihood of adequately sampling the phase space, the temperature was set at 1000*K* using a Maxwell-Boltzmann distribution. The time step for all simulations was set at 0.5 *fs*. Calculations were initialised with V atoms in ferromagnetic order.

2.3. Structure generation

We collected training data from two different supercells of $Na_xV_2(PO_4)_3$ (Na_xVP). The first structure contains 2 f.u. of NVP, with four vanadium atoms, and the second structure is the $2 \times 2 \times 2$ cell, containing 32 vanadium atoms.

Within the NASICON framework, two crystallographic Na-sites are reported: Na(1), and Na(2). The Na(1) site is located in a $[V_2(PO_4)_3]$ unit along the c-direction, with 6 oxygen neighbours, while Na(2)-ions are surrounded by eight oxygen atoms in its first coordination sphere [36,37]. A f.u. of NVP contains one Na that occupies a Na(1) site and two Na that occupies the Na(2) site. The calculated Na-O distance at the Na(1) site, has been found to be 2.378, which is much shorter than the average Na-O distance at the Na(2) site of 2.521 [38]. Due to the shorter Na-O distance, the Na(1) site is more stable and calculations reveal that the Na occupancy energy at the Na(1) site is 130 $meV/f.u.$ lower compared to those of Na(2). [33]. Therefore, during deinteracalation, the occupancy of Na(2) decreases, while the occupancy of the Na(1) site remains close to 1 [39].

The initial structures for Ab-initio molecular dynamics (AIMD) had sodium concentrations varying from $Na_x = 0$ to $Na_x = 3$. To improve variability in the training sets, the Na (1) and Na (2) sites were randomly populated at a given Na concentration.

When MD was performed with an ensemble of ML models, initial structures were created by employing a basin hopping algorithm on the 300 atom supercell at various Na concentrations, using the ML-ensemble as a calculator. Sodium ions were populated, so that Na(1) sites were filled first, followed by Na(2). Sodium concentration was varied from $Na_x = 1$ to $Na_x = 3$, and the volume of the cell was increased linearly from $Na_x = 1$ to $Na_x = 3$, following previous work [36].

2.4. Force and energy predictions - equivariant graph neural network model

Recently developed linear scaling message passing neural networks (MPNN) based interatomic potentials [24,40–43] are especially effective when many types of atoms are involved and the data sets are large. The conceptual idea behind these models is to represent a crystal structure or molecule as a graph, where each node in the graph corresponds to a atom in the system. Edges of the graph (atom-to-atom connections) are drawn where the atoms are within a certain cutoff distance, which is a hyperparameter of the model. The nodes of the graph have a "hidden" representation, which can be seen as a fingerprint representing the atom and its local environment. The nodes interact with each other through message passing steps. Information is exchanged between the nodes and the contents of these messages is modelled with artificial neural networks. The iterative exchange of information in principle enables an atom to influence atoms far away from its cutoff radius. After a number of message passing steps an energy contribution from each atoms is extracted with another neural network that maps each atom's hidden representation to a scalar value. The contributions are summed up to give the total energy. The message passing steps are all differentiable so forces can be obtained by calculating the gradient with respect to the atom positions. In the first generation of message passing algorithms, the hidden representations of the atoms are invariant with respect to rotation and translation of the molecules. However, this means that directional information is lost in the message passing [24,44]. In the new generation of equivariant message passing models [24,45–49] the hidden representation of the nodes is given the ability to retain directional information in, which improves the accuracy and data efficiency of the models [43]. The loss function considers both the total energy E, as well as forces $\mathbf{F}_i$ to accurately predict both properties:

$$\ell(\widehat{E}, (E, \mathbf{F}_1, \ldots, \mathbf{F}_n)) = (1-\rho)\| E - \widehat{E} \|^2 + \rho \frac{1}{n} \sum_{i=0}^{n} \| \mathbf{F}_i - \left(-\frac{\partial \widehat{E}}{\partial \mathbf{R}_i} \right) \|^2 \tag{1}$$

It should be pointed out that the accuracy of the ML models rely on high-quality DFT data, for example, from dense k-point sampling, large enough plane-wave energy cutoff and higher rung functional like HSE06. For deploying our methods in novel materials to discover unknown phenomena, it is required that data is collected with DFT after performing convergence tests on these parameters. For the simulations described in this article, we did not try to verify the convergence of the energy and forces of the DFT calculations but took the suggested energy cutoff for accurate simulation for the hardest pseudopotential (oxygen).

In this work, we use our own implementation of message passing equivariant graph neural network following similar published work [24]. Other models have also been used to study NASICON materials, such as kinetic Monte Carlo (kMC)[50]. kMC is a lattice based model where the possible events are predefined but it allows us to study diffusive processes in cathodes at micrometre and millisecond scales. In contrast, ML force fields compute forces and energies continuously as a function of atomic positions allowing the possibility to observe unexpected phenomena and provide structural distortion details for out-of-equilibrium motifs as well. Our novel GNN approach gives us access to electronic degrees of freedom as well. Thus in the ML accelerated multiscale simulation [15,51] paradigm of battery materials, our models operate at a lower time and length scale than kMC and compliments it. kMC input parameters like accurate diffusion barriers need to implicitly account for structural and electronic changes during diffusion. Typically such barriers are obtained from DFT calculations. For large systems with many structural and configurational degrees of

freedom, the number of barrier calculations can be in the thousands and require large simulation boxes. This being infeasible, low-accuracy approximations [52] are often done - lowering the reliability of the results from kMC simulations. We envision that our ML models complement kMC method by enabling large scale high accuracy barrier calculations providing parameters to kMC on the fly.

We implemented an ensemble of models consisting of four individual models with different sets of hyperparameters, while the predictions were given by the ensemble average. The uncertainty was estimated by the variance of the model predictions in the ensemble [53]. The prediction uncertainty was later applied within the active learning framework. Due to the nature of the numerical procedure of DFT simulations, total energies are well converged while forces obtained are noisy and force accuracy depend on high converged DFT parameters which is not possible to adhere to for large scale data collection like ours. Noise in force data makes it harder to train for accurate force prediction although error-free propagation of MD simulations depends on high accuracy forces. Thus our model training required a higher proportion of force loss. From one DFT data point, we have one energy observable but many force observables (one vector per atom) making force loss coefficients on the order of 100–1000 times larger than energy loss coefficient [24,54]. All models were therefore initially trained with a force weight $\rho = 0.99$, and interactions between atoms were considered within a cutoff radius $r_{cut} = 5$. All models were trained with a stochastic gradient descent, using the ADAM optimizer[55], and an initial learning rate of $\eta = 10^{-3}$. A validation set consisting of $\sim$ 1% of the data was used for early stopping. The models used in this study are listed with their hyperparameters in Table 1.

2.5. Charge predictions with density scanning nodes

To track the oxidation state of vanadium, we use an up- and down-spin electron density prediction model trained on the charge density outputs (CHGCAR) of the ab initio calculations. Starting from our recently developed equivariant DeepDFT model [56,57], we extend it to predict two outputs, (a) the total electron density and (b) the difference between the up and down spins. The charge(spin) density model is also based on a message passing graph neural network model and it uses the same form of equivariant internal node representations as the model described above.

The fundamental difference is that, in addition to the atom nodes, special probe nodes are inserted, which only receive messages in the message passing process and, therefore, do not affect the representation of the atom nodes. These probe nodes allow the electron density to be predicted at any point in 3D space even though the training data is given on a grid. For each gradient update in the training phase, two structures are sampled and 1000 grid points are sampled within each structure. The mean squared error between the prediction and the reference data is used as the cost function (Fig. 2).

During training, we utilize observations of density at discreet points as training data. As the underlying function is continuous and differentiable, we can sample from DFT done with any real space grid, even non-uniform grid spacing or simulations done with different grid spacings. The benefit of having a continuous function for density is that during inference we can output density over any grid spacing irrespective of that for the data used to train. For very large-scale simulations our model allows us to describe density around only a specific

Table 1
Hyperparameters of the 4 models we trained during this study.

Model	Embedding size	Interaction layers
Model 1	128	3
Model 2	148	3
Model 3	128	4
Model 4	148	4

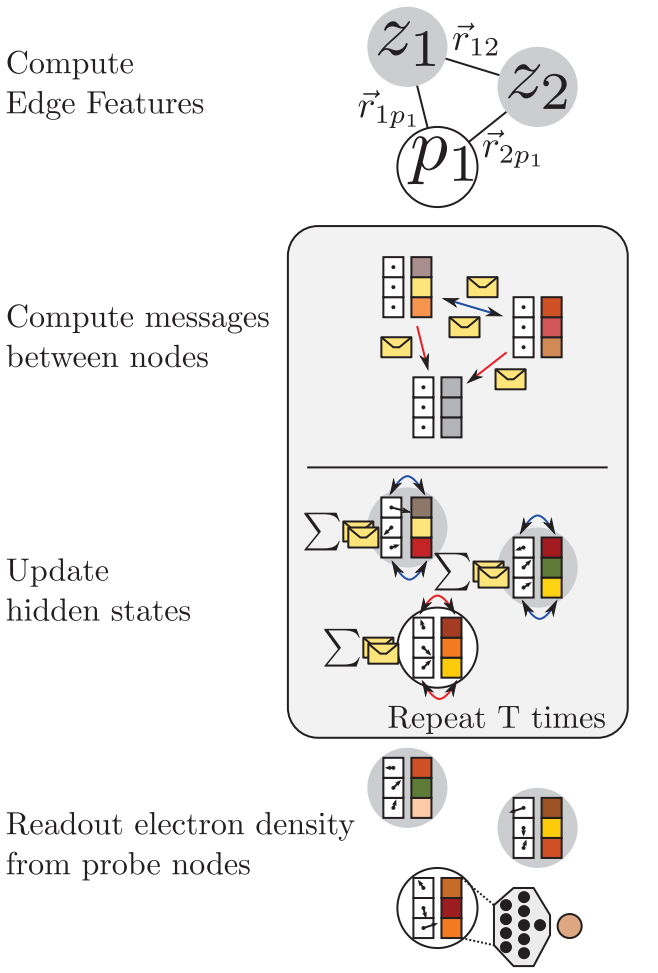

Fig. 2. In the charge density prediction model message passing scheme we compute interatomic messages in multiple interaction steps and then calculate the density at each query point.

focus atom or region of interest. We want to emphasize that the DeepDFT model, can generate charge density on selective local snapshots independent of the underlying machine learning potential employed. As a result, it can be integrated with other models of energy/force prediction that drives the molecular dynamics. For systems with simpler electronic structure, one can use this flexibility to simulate larger system faster with another model like [3,17,58] and infer electron density only for the steps that are deemed interesting.

We implemented a single charge density model in this work, initialised with 3 interaction layers and an embedding size of 128.

2.6. Collecting training data with on the fly learning

For the initial training set, AIMD was performed for 30 different initial configuration based on number of Na atoms and their ordering, run for 500 steps each, giving a total of 15000 individual structures. Once the initial model ensemble was trained with this data, it was used for MD. During this first deployment of the ML ensemble, as the structure evolved, the force variance between models started to increase rapidly after $2 - 10\ ps$. When force variance increased above $5\ eV/$, we found that the simulation broke down quickly due to unphysical forces, usually after less than 10 time-steps.

When structures are outside the distribution of the training data, force predictions are unreliable. To obtain an accurate description for the PES, we would need to collect a large variety of long time scale AIMD simulations. As we are limited by the high computational cost of

obtaining training data, we have to intelligently sample unknown parts of the PES. To tackle this problem, we developed an active learning framework inspired by Wang [17], and Botu [59]; First, we created an initial structure and ran MD, employing the ML ensemble for energy and force predictions. During the dynamic evolution of the structure, the active learning framework was conditionally activated. If the force variance between the models was in the range $1\ eV/ < f_{var} < 5\ eV\ /$ the configuration was added to the training set, and the simulation was continued. To avoid adding nonphysical structures to the set, we added the constraint that structures with variance larger than $5\ eV\ /$ were kept out of the set. It is worth mentioning that active learning is a general method for optimal data collection while building ML potentials that rely on predicted uncertainty for new structural configurations to choose which one to be calculated with DFT. Active learning strategy allows models to be built in a data efficient manner while achieving high accuracy. Similar methods to ours using uncertainty between ensemble models have been used previously, for example in moment tensor potentials [17,60,61], GAP potentials [22,62] and graph neural networks [63].

We initialised 5 different structures, at different sodium concentrations, on the 2 f.u. supercell and applied the above process with the trained ensemble. In total, 214 different structures were collected. For each of the structures, an AIMD simulation ran for 25 time steps, at $T = 1000\ K$ with a step size of $0.5\ fs$. The ML ensemble was then retrained on this new dataset. Previous work, showed that progressively increasing the energy loss coefficient during training was an effective strategy for reducing training time [64]. Therefore, we reduce ρ to $\rho = 0.9$ during this phase of training. By sampling the space in this way, the ML ensemble eventually gathers enough information about the PES, and can perform MD with sufficient accuracy on a long timescale. In this work, the process is repeated until the ML ensemble can perform *ns* molecular dynamics for the 16 f.u. supercell.

As we are interested in studying a larger system allowing symmetry breaking and novel structure/electronic motif to emerge, we expand the original 2 f.u. cell in a $2 \times 2 \times 2$ cell supercell with ~ 300 atom. We then apply the retrained models to perform MD on the larger structure. When the MD leads to high-variance structure and the MD breaks apart, we repeat the active learning framework with 5 different structures of varying sodium concentrations. After retraining the models on this final dataset, we performed a qualitative test on the fully sodiated 16 f.u. supercell, with the ensemble models. The simulations ran for more than 1 *ns*, without the structure becoming non-physical or breaking down.

Finally, MD based active learning as performed here, is not the only suitable way to collect large amounts of training data. Machine learning models perform optimally, as long as the phase space of the training set is large and includes structural motifs that are similar to those encountered during the deployment phase. For studying ionic diffusion with our method, it is essential that we capture many different types of ionic jumps, even rare ionic jumps in our training set. Many materials exhibit "sparse" diffusion in the sense that only a small subset of diffusion events contribute to the diffusivity [65]. This can be problematic, as the timescales to observe such events using MD are often on mu - ms timescales. In this case, a more suitable method for gathering training data, would be to also utilize nudged elastic band (NEB) based data collection for training, as NEB has the added flexibility of specifying the trajectory the ions move and track very rare events with large barriers.

For Full details of the iterative training including training curves, please see appendix A (for force/energy) and B (for charge density training) in supporting information.

3. Accuracy of the models

3.1. Accuracy of forces and energy

Once we have a set of fully trained models, we need to quantify their accuracy. Several reports in the literature report accuracy based on the validation set [17], or on data which the models are trained on. However, this underestimates the error of the model, as they have already seen the data [66]. To give an unbiased sense of the accuracy, we created a separate data set that the models had not seen, which contains ~ 1200 data points of the AIMD data at 1000 *K*. The initial configuration was created by removing two sodium atoms from the 2 f.u. supercell. The error distribution for forces and energy is shown in the top part of Fig. 3

The mean absolute error (MAE) on the test set was found to be 0.23 $eV/$ and 1.52 $meV/atom$ for forces and energy, respectively.

3.2. Accuracy on charges

Here we are interested in understanding how the oxidation state of vanadium changes dynamically. As the cathode is cycled from $Na_3V_2(PO_4)_3$ to $NaV_2(PO_4)_3$, *V*-ions can be in two different oxidation states; V^{3+}, and V^{4+} [67].

To distinguish between different oxidation states, we integrate the DFT-based and predicted charge densities according to Bader partitioning [68]. For the *V* ions, this gives a distribution of charge around two different charge centres, where each centre corresponds to either V^{3+}, or V^{4+}. This can be seen in Fig. 3c), where the Bader charge difference between the two centres is ~ 0.25. The model predicts a distribution similar to the one predicted by DFT.

If we look at the error distribution in Fig. 3b), we see that most errors are less than 0.05. MAE of the density model was found to be 0.009. This is much less than the separation between different oxidation states of *V* ions, indicating that the DeepDFT type model can accurately capture differences in oxidation state during dynamics.

3.3. Accuracy of reaction barriers

To verify the ability of the ML-ensemble to model the PES accurately during diffusion of Na-ions, we use the Nudged elastic band (NEB) method [69]. Previous reports have found that a concerted Na(1)-Na(2) ion exchange may be the preferred diffusion route in the structure [38]. We define a similar trajectory shown in the right side of fig 5 as input to the NEB calculations. We repeat the calculations at two different sodium concentrations, $Na_x = 2$ and $Na_x = 2.5$. Vacancies are created by removing Na from the Na(2)-site. Calculated NEBs for ML and DFT are shown in Fig. 4 a), and b). With the same initial and final state, the ML ensemble model found practically the same NEB path and associated barrier as DFT. This indicates that the ML ensemble can model the PES, during complex concerted ion diffusion.

4. Results and discussion

4.1. Diffusion mechanism

To understand ion mobility in $Na_3V_2(PO_4)_3$, MD was performed in the canonical NVT ensemble with a timestep 0.5 *fs*, using the ML ensemble, in the 16 fu supercell (~ 300 atoms). Before MD was run, each structure was optimised with a basin hopping algorithm for 100 steps. Sodium concentration in the structure was varied from Na_3VP to Na_1VP, and 4 different temperatures were investigated $T \in [300K, 400K, 500K, 600K]$. We ran MD at elevated temperature for collecting training data whereas we reduced the temperature when running the actual simulations for three reasons. By increasing the temperature, we sample a larger variety of configurations away from the equilibrium. This diverse data helps the ML model be more robust and generalize better. Secondly, the cost Of AIMD based acquisition of data with dissimilar structures can be lowered if new structural motifs are visited during MD quickly and frequently. This is achieved by running the MD at a higher temperature, as the high kinetic energy drives the system away from the equilibrium structure. Third, by lowering the temperature during inference, the atomic neighbourhoods encountered are not out of distribution from the

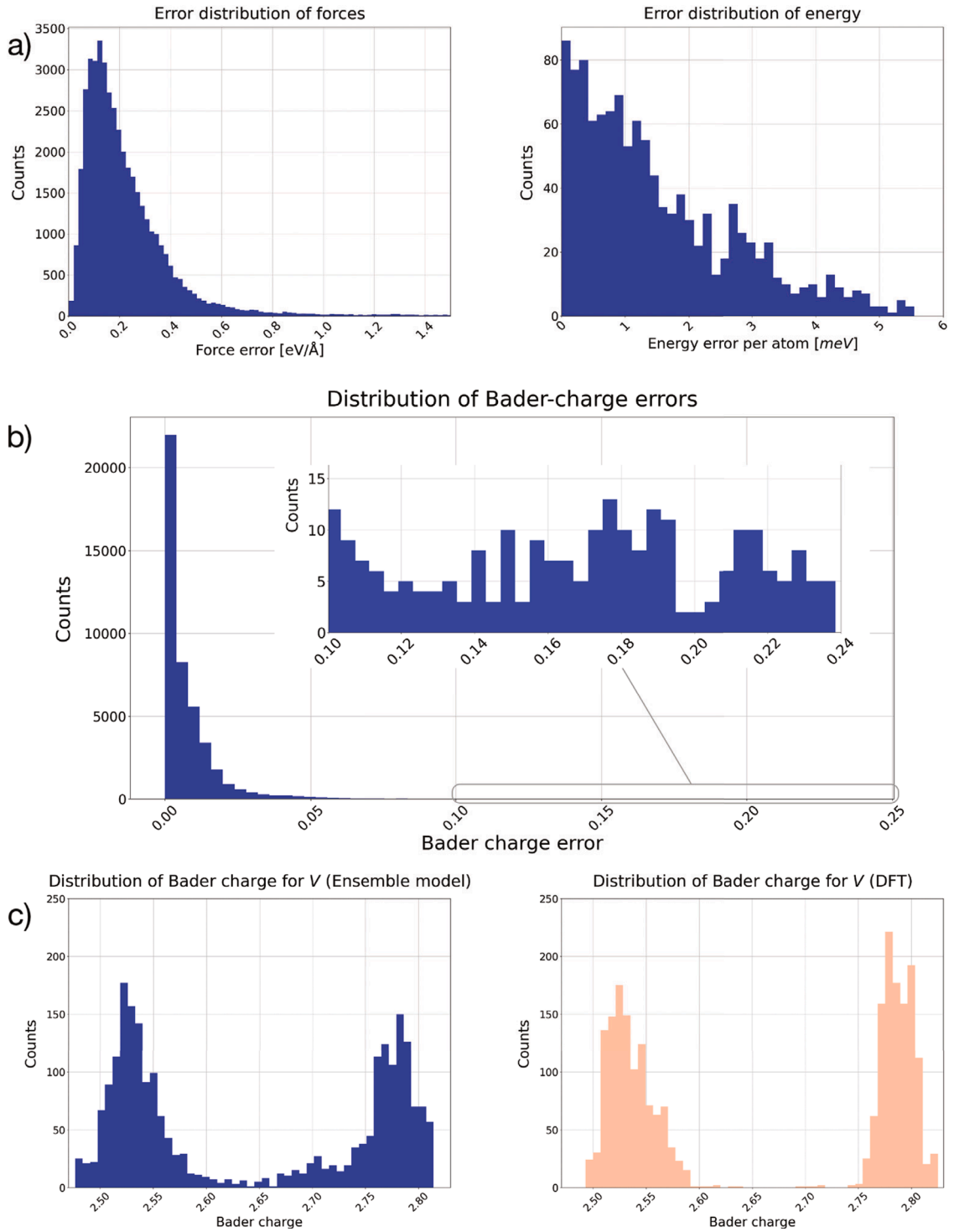

Fig. 3. a) Error distribution for the final fully trained ensemble model on force, and energy predictions [per atom] b) Error distribution for predicted Bader charge found by integrating the model derived charge densities, and comparing with DFT. c) Distribution of Bader charges for Vanadium atoms, predicted from the ensemble model (left), and DFT (right).

training data and thus the model has low error and the MD run is stable providing more accurate results. If we run MD at higher temperatures, such as 1000*K*, the models quickly encounter structures with atomic structure neighbourhoods that are out of distribution from training data leading to high prediction uncertainty. As we observe statistically plentiful diffusion phenomena at 400*K*, we chose to limit the maximum temperature to 600*K* to improve the accuracy of our predictions.

Each trajectory was run for a single day on a NVIDIA RTX-3090 graphics card, without specifying a time limit for the MD simulations. This produced a distribution of different length scales, and the median time each simulation was run was 166 *ps*. In total, data from more than > 30 *ns* of MD are collected, and during all simulations, only Na-ions are observed to diffuse from their equilibrium position.

As mentioned above, the NASICON structure has two distinct Na sites. The first is the Na(1) site, which is the most stable and is surrounded by 6 oxygen atoms, while the Na(2) site has an 8-fold

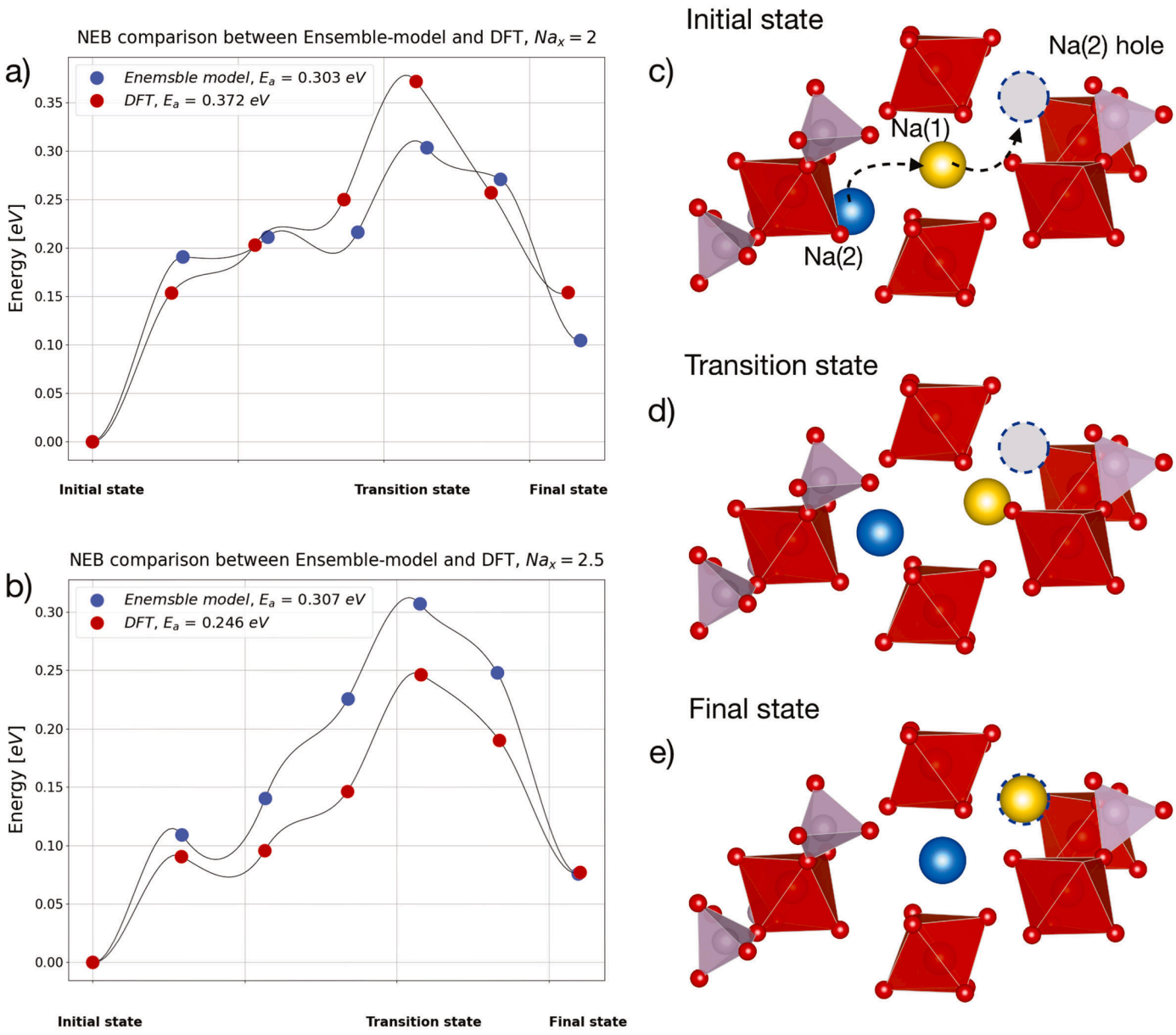

Fig. 4. a) Comparison of the predicted NEBs, using the ensemble model [blue], and DFT [red] at the sodium concentration $Na_x = 2$. b) Comparison of the predicted NEBs, using the ensemble model [blue], and DFT [red] with the same trajectory, at a sodium concentration $Na_x = 2.5$. c) Geometry of the initial state, illustrated with the prescribed diffusion pathway. d) Atomic arrangement of the transition state of the NEB trajectory. e) Final atomic arrangement of the NEB trajectory. (For interpretation of the references to colour in this figure legend, the reader is referred to the web version of this article.)

coordination and longer Na-O distances. From the simulations, only a single diffusion phenomenon was observed; Na(1) - Na(2), or Na(2) - Na (1).

The observed diffusion process occurs in two steps. (i) A Na(1) ion moves into a vacant Na(2) site, leaving a nascent vacancy at the Na(1) site (ii) A neighbouring Na(2) ion quickly migrates, filling the Na(1) vacancy and create a vacancy at the Na(2) site. The mechanism is illustrated in Fig. 5. Both concerted ion exchange and standalone Na (1)⟶ Na(2) diffusion have been studied previously and shown to have a ∼ 5 times lower activation barrier than a direct Na(2)-Na(2) diffusion pathway [38,67]. This suggests that both the Na (1) and Na (2) ions are mobile during diffusion, which is also captured by the ML ensemble.

To determine if concerted ion motion, is the dominating diffusion pathway in NVP, we determined the number of collective jumps as a function of temperature. Jumps were considered concerted if the time difference between jumps, was on the same order of magnitude as the attempt frequency [70]. Following previous work studying diffusion in superionic conductors, jumps were considered concerted if they occurred within 1 ps of each other [71]. The results for concerted ion jumps were subsequently compared to the total number of jumps, revealing that the number of collective jumps depends strongly on the temperature. At temperatures above 400*K*, our results show that concerted ion motion is the dominating diffusion pathway in the structure. At 400*K*, roughly 48% of ionic jumps are concerted, increasing to 57% at 500*K* and 67% at 600*K*. Thus collective jump processes may have a significant effect on Na-ion diffusion inside NVP, especially at elevated temperatures. The increase in the percentage of concerted ion jumps as a function of temperature, is likely caused by the higher number of jumps at elevated temperatures, as Na-ions will be influenced by other moving neighbouring Na-ions, thus increasing the probability of collective ion motion [70] (Fig. 6).

Additionally, our results indicate that Na(1) sites are vacant only during short transitionary periods, thus Na(1)-occupancy remains close to 1 as sodium is deintercalated, in agreement with previous findings

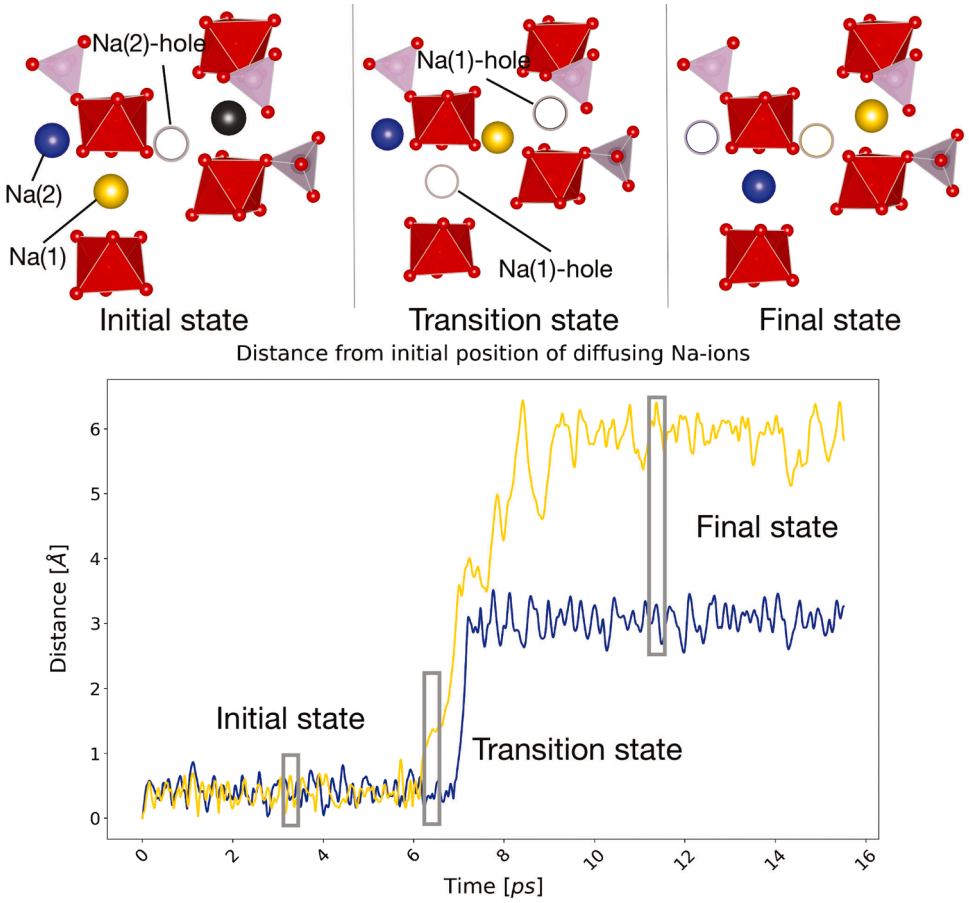

Fig. 5. Schematic of the concerted ion exchange which occurs during diffusion of *Na*-ions. Initially a Na(1) ion(yellow) migrates to a vacant Na(2) site. Once the migration has taken place, a hole is left at the Na(1) site, which is quickly filled by a neighbouring Na(2)-ion. Thus migration of ions in the structure occurs through a joint Na(1)-Na(2)-Na(1) diffusion scheme. (For interpretation of the references to colour in this figure legend, the reader is referred to the web version of this article.)

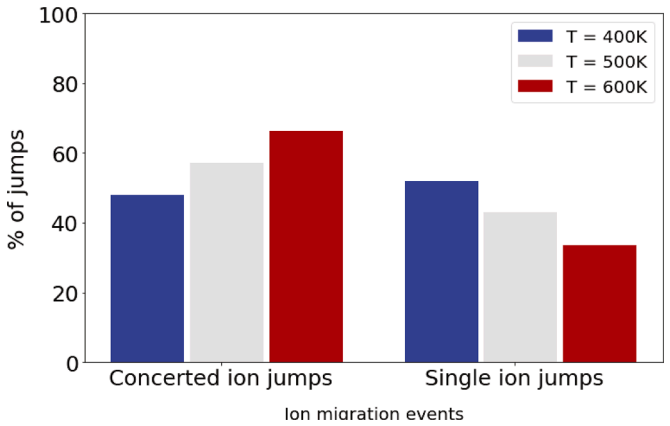

Fig. 6. Distribution of concerted and single ion jump events as a function of temperature.

[39]. As both Na(1) and Na(2) are essential in the migration process, we expect no diffusion at sodium concentrations below $Na_x = 1$ (Na_1VP), since all Na ions will be located at the energetically favourable Na(1) site.

We want to touch upon two critical points, regarding the application of the model. Firstly, our model can be used for simulating very large scale systems for long trajectories as the computational cost increases linearly with the system size, unlike DFT. The current implementation is limited to the accessible GPU memory for system size that can be worked with. e.g. with the model hyperparameter we have used 3000 atoms can be simulated with a 3090RTX GPU with 24GB memory. Nevertheless, due to the many configurations, ion-concentrations and temperatures we investigated, our GNN based MD computations took ∼ 300 GPU-days with the ∼ 300 atom system size we chose. Our goal for this research was to demonstrate ∼ ns length scale simulations with electron density description, that allow us to investigate diffusion behaviour and the associated redox processes at many different Na-concentrations within a reasonable timeframe and the accessible GPUs. Our models are adaptable to larger systems of thousands of atoms and even longer time scales than we did, if fewer systems to be simulated or larger compute resources are available

Secondly, none of our MD simulations makes assumptions about different diffusion paths inside the structure. Taking into account the complexity of concerted ion migration, it is notable that our ML model predicts concerted ion movement as the dominant diffusion pathway, similar to previous results in the literature [38]. This demonstrates that ML-models are capable of predicting diffusion pathways, even in challenging systems, such as NASICONs.

4.2. *Diffusivity at different concentrations and temperatures*

Diffusivity of Na-ions was calculated by counting the number of ions migrating during a given time period normalized by the number of Na-ions in the structure, denoted by Γ in this study. The diffusion coefficient was then found by linking the ion migration rate, to the average distance d_{ion} an ion jumps:

$$D(Na) = \frac{1}{6} d_{ion}^2 \Gamma \tag{2}$$

Migration was considered when a Na-ion moved further away than 3 from its initial position. To obtain better statistics, 3 different initial configurations were considered when MD was run at a given Na concentration. The diffusion coefficient at a specific concentration was found by averaging the diffusion coefficients from the 3 MD simulations. We investigated diffusion in 4 different temperature regimes; $T \in [300K, 400K, 500K, 600K]$. Although nothing prohibited us from going up to higher temperatures, such as $1000K$, the models quickly encounter structures with high prediction uncertainty at higher temperatures. As we observe plentiful of diffusion phenomena at $400K$, we chose to limit the maximum temperature to $600K$ to improve the accuracy of our predictions.

In Fig. 7, we have presented the diffusivity as a function of concentration and temperature, for the case of high discharge rates. At high discharge rates, the system does not have enough time to reach a thermodynamic equilibrium and therefore remains in a solid solution during discharging. However, at slower discharge rates, the system exists in a two-phase region at $1 < Na_x < 2$ and $2 < Na_x < 3$ [36]. As a result, at slow discharge rates, diffusivities should be considered as an average of the diffusivities in the single-phase regions.

At a temperature of $T = 300K$, Na ions simply vibrate around their equilibrium position. The diffusion of ions was only observed at two different concentrations; $Na_x = 2$ and $Na_x = 2.75$, with only a single ion migration event occurring at this temperature. As predicted by the Arrhenius equation, ion migration increases sharply with temperature. The maximum diffusivity is found at $T = 600K$, at the concentration $Na_x = 2.75$, with $D_{Na} = 2.1\ 10^{-6} cm^2/s$. At $T = 600K$, the diffusivity decreases almost two orders of magnitude from $Na_{2.875}V_2(PO_4)_3$ to $Na_{1.25}V_2(PO_4)_3$, with similar trends observed at $T = 500K$. Therefore, the activation barrier for Na-ion diffusion is highly dependent on Na concentration. To investigate the Na concentration dependence of diffusion, we looked at two different concentration regimes. First, when it is close to fully charged, $Na_x, x \in 2.875.2.75$ and when it approaches 50% SOC $Na_x, x \in 2.25.2.125$ To find the activation barrier, we assume that diffusivity D_{Na} can be described in terms of the Arrhenius relation as [72]:

$$\log(D_{Na}) = \log(D_0) - \frac{E_a}{k_B T} \tag{3}$$

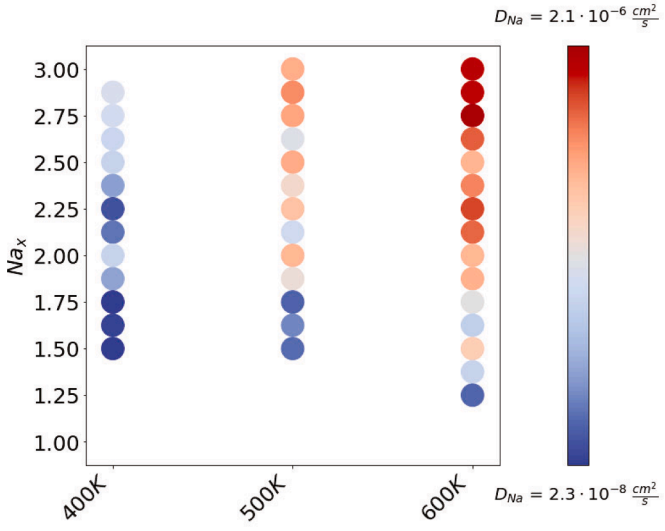

Fig. 7. Logarithm of the diffusion coefficient, as a function of concentration; Na_x and temperature. Spots without dots, indicate no ion migration was observed during the simulations at a given concentration.

Where E_a is the activation barrier for ion migration, k_B is the Boltzmann constant, and D_0 is the preexponential coefficient. The plot of the logarithm of D_{Na} versus $1/T$, should result in a linear relationship. The Arrhenius-type plots are shown in Fig. 8, and indeed a good linear fit between diffusivity and inverse temperature is found. Activation barriers are determined from the slopes of the curves, in Fig. 8, and are shown in Table 2.

The activation barriers determined from previous NEB-DFT calculations were found to be $0.304eV$ at $Na_3V_2(PO_4)_3$ [67]. This is similar to our results of $0.23eV - 0.26eV$, determined from MD, indicating that properties such as the ion migration rate can be accurately determined using machine learning models. Furthermore, our MD has allowed us to study, for the first time, the dependence of activation barriers on sodium concentration for a wide range of sodiation levels. Interestingly, we observe that the activation barrier almost doubles when the sodium concentration reaches $Na_x = 2.25$. This can be rationalised in terms of the probability of finding sodium pairs for concerted diffusion, which decreases as sodium is extracted from the material.

Our models predict a smaller barrier at high sodium concentration, compared to previous results, and hence a faster diffusion rate. The error may be explained by the lower energy loss coefficient employed here, which is more biased towards predicting correct forces than energies. It is important to note however, that the errors in barriers should be evaluated in the context of the differences in barriers calculated from various DFT calculations. For instance, previous research of the lowest diffusion barrier for the hole-polaron in Li_2O_2 calculated using HSE with $\alpha = 0.25$, ranges from 0.038 [73] to 0.068 eV [74], while using $\alpha = 0.48$ yields a barrier of 0.42 eV [73]. Thus minor changes only in the exchange-correlation functional can lead to changes in predicted barriers up to 0.3 eV. As our ML models are trained with data from PBE+U calculations ML simulations are expected to follow a similar trend and deviate from other DFT based barrier calculation results done with HSE06 functional [34]. Simulation results from our PBE+U based surrogate potential are reasonably close to previous results and satisfactory considering we calculate the activation energy using MD with an ML potential, whereas most authors use DFT-NEB methods.

An interesting investigation is to determine the contribution of ionic jumps to the overall macroscopic diffusion. It should be noted that not all Na-ions contribute to macroscopic diffusion as they may return to their original positions. To determine if most jumps contribute to macroscopic diffusion, we can compare the diffusivities calculated from the ionic jumps (Eq. (2)) denoted D_{Jump} to diffusivities calculated from mean squared displacement of Na-ions denoted as D_{MSD}:

$$D_{MSD} = \frac{1}{6N} \Sigma_i^N |\mathbf{r}_i(t) - \mathbf{r}_i(0)|^2 \tag{4}$$

Fig. 9 illustrates a plot of D_{MSD} and D_{Jumps} at $T = 600K$. From the figure, it is observed that the D_{Jumps} follows the same trend as D_{MSD}. However, at specific Na-concentrations, such as $Na_x = 1.875$ and $Na_x = 1.5$, the jump rate coefficient is overestimated. This suggests that at certain concentrations, the ionic jumps do not significantly contribute to macroscopic diffusion. Nevertheless, in general, the jumps determined from D_{MSD} and D_{Jumps} are of the same order of magnitude, leading us to propose that the majority of ionic jumps inside the structure contribute to overall macroscopic diffusion.

Our research has revealed two significant findings. Firstly, at high Na-concentrations, diffusivity is the highest. Secondly, as the Na-concentration is reduced, diffusivity decreases substantially. This decrease in diffusivity can be attributed to three key factors.

First, as the sodium concentration is reduced, the concentration of Na (2) ions decreases. As a result of the reduction in Na(2) ions, ion migration becomes increasingly difficult because both Na(1) and Na(2) ions must be present for ion exchange to occur.

Second, as the sodium concentration is reduced, the cell contracts, leading to a decrease in the Na-V distance, while at the same time more

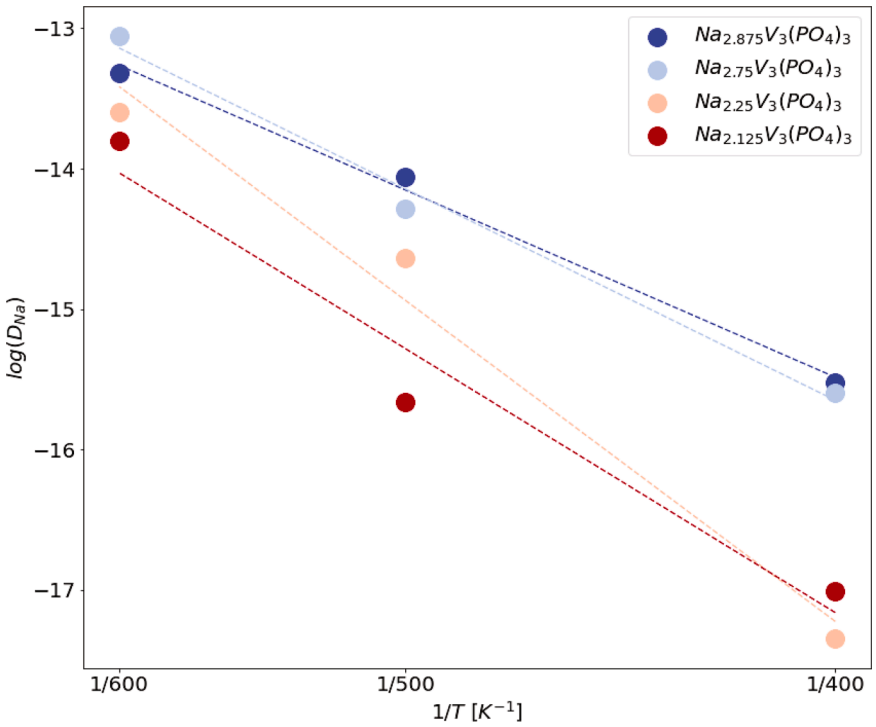

Fig. 8. Arrhenius plot of the logarithm of diffusivity versus $1/T$, for three different temperatures, and 4 different Na-concentrations. Dashed lines shows the fitted curve, at a given Na-concentration.

Table 2
Activation barriers for Na-ion diffusion at different Na concentrations.

	$Na_{2.875}$	$Na_{2.75}$	$Na_{2.25}$	$Na_{2.125}$
E_a	$0.23eV$	$0.26eV$	$0.39eV$	$0.33eV$

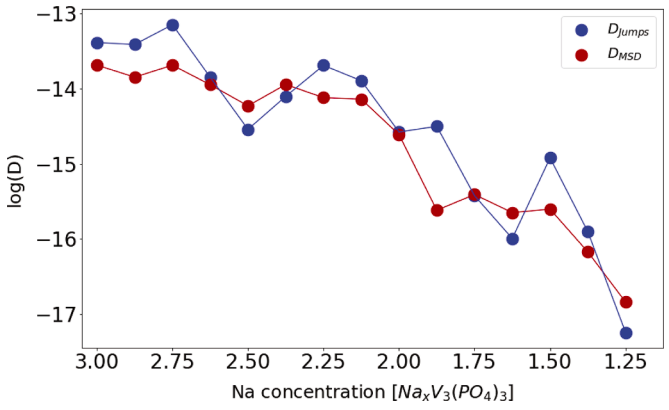

Fig. 9. Plot of Na-ion diffusivity calculated from Na-ion jumps [blue] (Eq. 2) and from the mean squared displacement [red] (Eq. 4), at T = 600K. (For interpretation of the references to colour in this figure legend, the reader is referred to the web version of this article.)

and more V ions change the oxidation state, from V^{3+} to V^{4+}, leading to an increase in electrostatic repulsion and greater destabilisation of the Na(2) site [67].

Lastly, during the deintercalation of Na-ions, the structure undergoes phase transitions. Previous findings revealed that the material exhibits different phases at varying sodium concentrations, with regions that are stable over a wide temperature range ($0K - 800K$). The authors found that the ground state configuration of Na_3VP was monoclinic ($C2\ /c$), Na_2VP was triclinic ($P1$), and Na_1VP was rhombohedral ($R3\ /c$) [36]. The end members Na_3VP, and Na_1VP are stable, while Na_2VP is metastable. At the structural level, Na_2VP is orientated so that Na (2) ions are located close to V^{3+} ions and, preferably, farther away from V^{4+} ions.

4.3. Vanadium charge ordering during ion migration

Previous investigations have shown that ion diffusion may be accompanied by a polaron migrating with Na vacancy [34]. To study the polaron-ion diffusion mechanism, we used our DeepDFT charge density prediction model to predict charge densities. Integration of the charge density according to Bader partitioning provides the oxidation state of the V-ions in the structure. The results from our MD simulations revealed the dominating diffusion mechanism, involved a concerted Na(1)-Na(2) diffusion mechanism. Hence, the oxidation state of V-ions is investigated during such a diffusion process.

Three different structures, at three different Na_x concentrations were investigated on the 16 f.u supercell; $Na_x = [2.875, 2.5, 2]$. The dynamic evolution of the polaron-Na diffusion process is illustrated for the case of $Na_x = 2.5$ in Fig. 10.

Charge exchange is observed to occur in three stages (i) Initially, V sites close to Na vacancies tend to be in an oxidation state of V^{4+}. (ii) As the first Na-ions migrate towards the Na-vacancies, the V^{4+} ions change oxidation state from V^{4+} to V^{3+} as seen in the middle of Fig. 10. The charge is transferred to a neighbouring V-ion, or the second nearest V-ion. During this transition, the polaron is not localised to a single site but jumps between different V-ions (iii) In the final state, as both ions have migrated to new equilibrium sites, vacancies are left at the original position of the Na(2)-ions. The V-ion closest to the nascent vacancy, is then oxidized, and remains as V^{4+}, as shown in the middle of figure.

Thus, Na-ion diffusion in the structure involves a transfer of electrons between V ions, and our results indicate that the electrons move in the opposite direction to the migrating Na-ions.

Earlier investigations have studied the diffusion process as a combined Na vacancy/polaron diffusion process. The authors used the HSE06 hybrid functional, which is very expensive, and found GGA+U methods to be less satisfactory in describing both polaron-diffusion

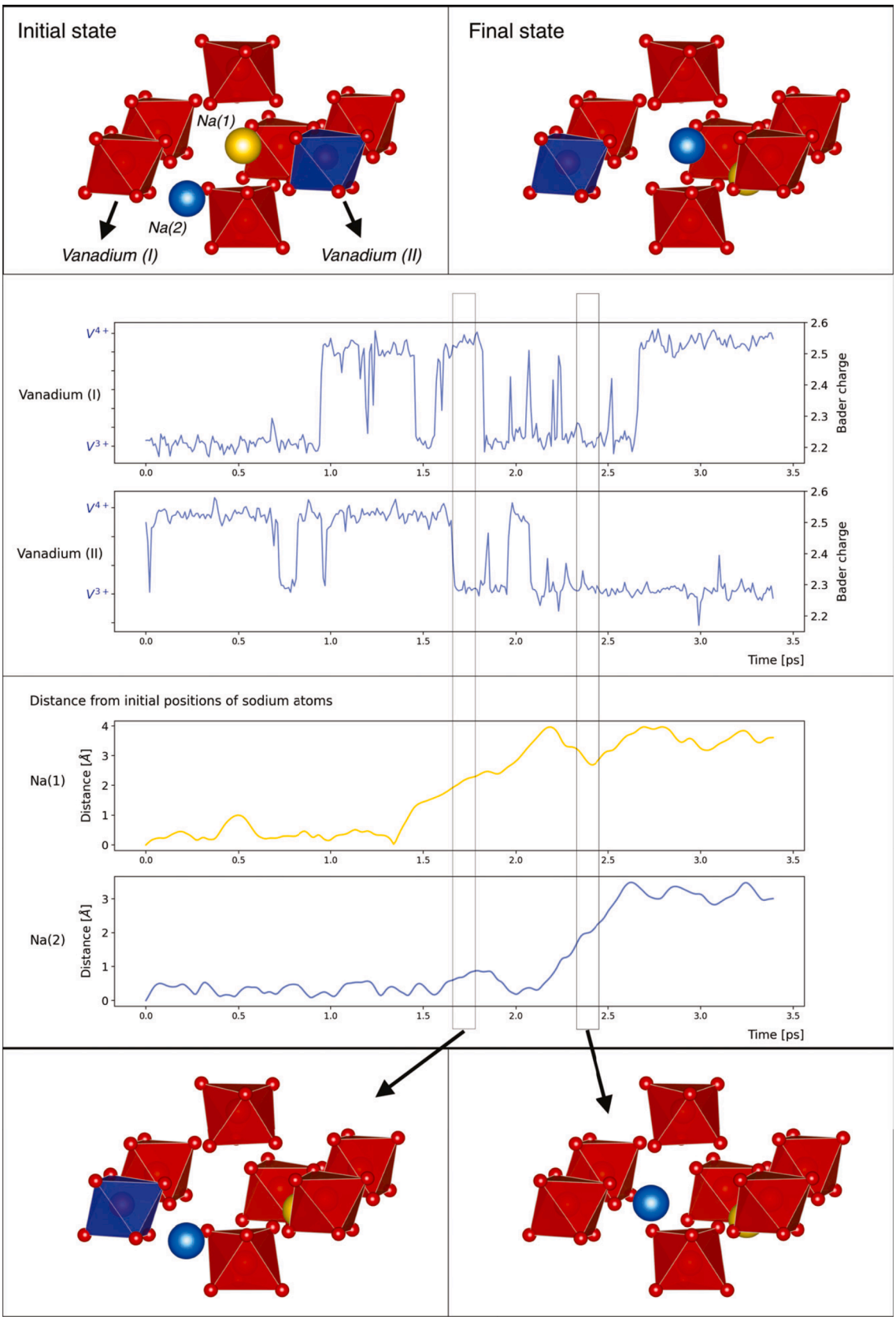

Fig. 10. Illustration of the model predicted bader charges of *V*-ions inside the structure, as *Na*-ion migration is occurring. Upper picture shows the initial state, and the final state of a concerted diffusion process. V^{4+} is shown in blue, and V^{3+} in red. The middle picture, shows the predicted Bader charge of *V*-ions, with the Distance from the initial positions of the migrating sodium ions. Bottom picture shows the transition state, during the diffusion process. (For interpretation of the references to colour in this figure legend, the reader is referred to the web version of this article.)

processes and the shrinkage of $V-O$ bonds, as V changes the oxidation state [34,75]. Results obtained from our spin-resolved charge density prediction model reveal that the average $V^{4+}-O$ distance, is 0.08 less, than the average $V^{3+}-O$ distance. This is in agreement with experimental data, since the difference in ionic radii between V^{3+} and V^{4+} is found to be 0.08 from Shannon tables. Thus, the DeepDFT model is capable of distinguishing different oxidation states of V ions.

5. Conclusion

In this work, an equivariant message-passing graph neural network model was successfully implemented to predict subatomic energies, forces, and spin-resolved charge density. This linear scaling model allows access to 100s of nanosecond of electronic scale MD simulation data with DFT-like accuracy. We used this machinery to investigate electron transfer coupled diffusion phenomena in a NASICON system of ~300 atoms, on the *ns* time scale, allowing a thorough investigation on the effects of sodium concentration on diffusion properties of Na-ions. Our results indicate that a concerted ion-exchange mechanism is the dominant diffusion pathway and show that our model can capture highly complex dynamics inside the structure.

By training an ML model on spin densities from DFT, we were able to investigate changes in electronic densities around vanadium ions during the migration of Na-ions. Our results indicate that the migration of Na-ions is linked with redox processes.

These findings serve as successful proof of concept of using equivariant graph neural network-based (energy, force, and charge density) surrogate models in studying electronic scale electrochemistry of complex transition metal oxides and polyanions. Given that the time spent in ML calculations is 3–4 orders of magnitude lower than DFT, it should now be possible to accurately study large and complex systems on nanosecond time scales. The workflow employed here can be easily expanded to different kinds of structure and chemistries.

CRediT authorship contribution statement

Paolo Vincenzo Freiesleben de Blasio: Data curation, Formal analysis, Investigation, Validation, Visualization, Writing – original draft, Writing – review & editing. **Peter Bjørn Jorgensen:** Methodology, Software, Writing – review & editing. **Juan Maria Garcia Lastra:** Supervision, Formal analysis, Investigation, Writing – review & editing. **Arghya Bhowmik:** Conceptualization, Supervision, Funding acquisition, Formal analysis, Project administration, Resources, Writing – original draft, Writing – review & editing.

Declaration of Competing Interest

The authors declare that they have no known competing financial interests or personal relationships that could have appeared to influence the work reported in this paper.

Data availability

All codebase, trained models, data from DFT simulations, and ML inference are shared via public repository https://zenodo.org/records/10051133.

Acknowledgement

The authors acknowledge financial support from Det Frie Forskningsråd under Project “Data-driven quest for TWh scalable Na-ion battery (TeraBatt)” (Ref. Number 2035-00232B) and from VILLUM FONDEN by a research grant (ref. no. 00023105) for the DeepDFT project.

Supplementary material

Supplementary material associated with this article can be found, in the online version, at 10.1016/j.ensm.2023.103023.

References

[1] Y. Elbaz, D. Furman, M. Caspary Toroker, Modeling diffusion in functional materials: from density functional theory to artificial intelligence, Adv. Funct. Mater. 30 (18) (2020) 1900778.
[2] J. Behler, M. Parrinello, Generalized neural-network representation of high-dimensional potential-energy surfaces, Phys. Rev. Lett. 98 (14) (2007) 146401.
[3] A.P. Bartók, M.C. Payne, R. Kondor, G. Csányi, Gaussian approximation potentials: the accuracy of quantum mechanics, without the electrons, Phys. Rev. Lett. 104 (13) (2010) 136403.
[4] J. Behler, Four generations of high-dimensional neural network potentials, Chem. Rev. 121 (16) (2021) 10037–10072.
[5] V.L. Deringer, A.P. Bartók, N. Bernstein, D.M. Wilkins, M. Ceriotti, G. Csányi, Gaussian process regression for materials and molecules, Chem. Rev. 121 (16) (2021) 10073–10141.
[6] B. Cheng, G. Mazzola, C.J. Pickard, M. Ceriotti, Evidence for supercritical behaviour of high-pressure liquid hydrogen, Nature 585 (7824) (2020) 217–220.
[7] V.L. Deringer, N. Bernstein, G. Csányi, C. Ben Mahmoud, M. Ceriotti, M. Wilson, D. A. Drabold, S.R. Elliott, Origins of structural and electronic transitions in disordered silicon, Nature 589 (7840) (2021) 59–64.
[8] N. Artrith, A. Urban, G. Ceder, Constructing first-principles phase diagrams of amorphous LixSi using machine-learning-assisted sampling with an evolutionary algorithm, J. Chem. Phys. 148 (24) (2018) 241711.
[9] J.-X. Huang, G. Csányi, J.-B. Zhao, J. Cheng, V.L. Deringer, First-principles study of alkali-metal intercalation in disordered carbon anode materials, J. Mater. Chem. A 7 (32) (2019) 19070–19080.
[10] M. Babar, H.L. Parks, G. Houchins, V. Viswanathan, An accurate machine learning calculator for the lithium-graphite system, J. Phys. Energy 3 (1) (2020) 014005.
[11] K.K. Rao, Y. Yao, L.C. Grabow, Accelerated modeling of lithium diffusion in solid state electrolytes using artificial neural networks, Adv. Theory Simul. 3 (9) (2020) 2000097.
[12] A. Marcolongo, T. Binninger, F. Zipoli, T. Laino, Simulating diffusion properties of solid-state electrolytes via a neural network potential: performance and training scheme, ChemSystemsChem 2 (3) (2020) e1900031.
[13] W. Li, Y. Ando, E. Minamitani, S. Watanabe, Study of Li atom diffusion in amorphous Li3PO4 with neural network potential, J. Chem. Phys. 147 (21) (2017) 214106.
[14] A. Bhowmik, M. Berecibar, M. Casas-Cabanas, G. Csanyi, R. Dominko, K. Hermansson, M.R. Palacin, H.S. Stein, T. Vegge, Implications of the BATTERY 2030+ AI-assisted toolkit on future low-TRL battery discoveries and chemistries, Adv. Energy Mater. 12 (17) (2022) 2102698.
[15] D. Diddens, W.A. Appiah, Y. Mabrouk, A. Heuer, T. Vegge, A. Bhowmik, Modeling the solid electrolyte interphase: machine learning as a game changer? Adv. Mater. Interfaces 9 (8) (2022) 2101734.
[16] G. Houchins, V. Viswanathan, An accurate machine-learning calculator for optimization of Li-Ion battery cathodes, J. Chem. Phys. 153 (5) (2020) 054124.
[17] C. Wang, K. Aoyagi, P. Wisesa, T. Mueller, Lithium ion conduction in cathode coating materials from on-the-fly machine learning, Chem. Mater. 32 (9) (2020) 3741–3752.
[18] M. Schreiner, A. Bhowmik, T. Vegge, P.B. Jørgensen, O. Winther, NeuralNEB-neural networks can find reaction paths fast, Mach. Learn. Sci. Technol. 3 (4) (2022) 045022.
[19] M. Schreiner, A. Bhowmik, T. Vegge, J. Busk, O. Winther, Transition1x-a dataset for building generalizable reactive machine learning potentials, Sci. Data 9 (1) (2022) 779.
[20] L. Kahle, A. Marcolongo, N. Marzari, Modeling lithium-ion solid-state electrolytes with a pinball model, Phys. Rev. Mater. 2 (6) (2018) 065405.
[21] L. Kahle, A. Marcolongo, N. Marzari, High-throughput computational screening for solid-state li-ion conductors, Energy Environ. Sci. 13 (3) (2020) 928–948.
[22] T.A. Young, T. Johnston-Wood, V.L. Deringer, F. Duarte, A transferable active-learning strategy for reactive molecular force fields, Chem. Sci. 12 (32) (2021) 10944–10955.
[23] O.T. Unke, S. Chmiela, H.E. Sauceda, M. Gastegger, I. Poltavsky, K.T. Schutt, A. Tkatchenko, K.-R. Muller, Machine learning force fields, Chem. Rev. 121 (16) (2021) 10142–10186.
[24] K. Schütt, O. Unke, M. Gastegger, Equivariant message passing for the prediction of tensorial properties and molecular spectra. International Conference on Machine Learning, PMLR, 2021, pp. 9377–9388.
[25] T. Jin, H. Li, K. Zhu, P.-F. Wang, P. Liu, L. Jiao, Polyanion-type cathode materials for sodium-ion batteries, Chem. Soc. Rev. 49 (8) (2020) 2342–2377.
[26] M.D. Slater, D. Kim, E. Lee, C.S. Johnson, Sodium-ion batteries, Adv. Funct. Mater. 23 (8) (2013) 947–958.
[27] J. Wang, Y. Wang, D.-H. Seo, T. Shi, S. Chen, Y. Tian, H. Kim, G. Ceder, A high-energy NASICON-type cathode material for na-ion batteries, Adv. Energy Mater. 10 (10) (2020) 1903968.
[28] M. Chen, W. Hua, J. Xiao, D. Cortie, X. Guo, E. Wang, Q. Gu, Z. Hu, S. Indris, X.-L. Wang, et al., Development and investigation of a NASICON-type high-voltage cathode material for high-power sodium-ion batteries, Angew. Chem. 132 (6) (2020) 2470–2477.

[29] S. Park, Z. Wang, Z. Deng, I. Moog, P. Canepa, F. Fauth, D. Carlier, L. Croguennec, C. Masquelier, J.-N. Chotard, Crystal structure of Na2V2(PO4)3, an intriguing phase spotted in the Na3V2(PO4)3-Na1V2(PO4)3 system, Chem. Mater. 34 (1) (2021) 451–462.

[30] G. Kresse, J. Furthmüller, Efficient iterative schemes for ab initio total-energy calculations using a plane-wave basis set, Phys. Rev. B 54 (16) (1996) 11169.

[31] P.E. Blöchl, Projector augmented-wave method, Phys. Rev. B 50 (24) (1994) 17953.

[32] J.P. Perdew, K. Burke, M. Ernzerhof, Generalized gradient approximation made simple, Phys. Rev. Lett. 77 (18) (1996) 3865.

[33] S.Y. Lim, H. Kim, R.A. Shakoor, Y. Jung, J.W. Choi, Electrochemical and thermal properties of NASICON Structured Na3V2(PO4)3 as a sodium rechargeable battery cathode: a combined experimental and theoretical study, J Electrochem Soc 159 (9) (2012) A1393.

[34] K.M. Bui, V.A. Dinh, S. Okada, T. Ohno, Hybrid functional study of the NASICON-type Na3V2(PO4)3: crystal and electronic structures, and polaron–na vacancy complex diffusion, PCCP 17 (45) (2015) 30433–30439.

[35] A.H. Larsen, J.J. Mortensen, J. Blomqvist, I.E. Castelli, R. Christensen, M. Dułak, J. Friis, M.N. Groves, B. Hammer, C. Hargus, et al., The atomic simulation environment–a python library for working with atoms, J. Phys.: Condens. Matter 29 (27) (2017) 273002.

[36] Z. Wang, S. Park, Z. Deng, D. Carlier, J.-N. Chotard, L. Croguennec, G.S. Gautam, A. K. Cheetham, C. Masquelier, P. Canepa, Phase stability and sodium-vacancy orderings in a naSICON electrode, J. Mater. Chem. A 10 (1) (2022) 209–217.

[37] B. Zhang, K. Ma, X. Lv, K. Shi, Y. Wang, Z. Nian, Y. Li, L. Wang, L. Dai, Z. He, Recent advances of NASICON-Na3V2(PO4)3 as cathode for sodium-ion batteries: synthesis, modifications, and perspectives, J Alloys Compd 867 (2021) 159060.

[38] Q. Wang, M. Zhang, C. Zhou, Y. Chen, Concerted ion-exchange mechanism for sodium diffusion and its promotion in Na3V2(PO4)3 framework, J. Phys. Chem. C 122 (29) (2018) 16649–16654.

[39] Z. Jian, C. Yuan, W. Han, X. Lu, L. Gu, X. Xi, Y.-S. Hu, H. Li, W. Chen, D. Chen, et al., Atomic structure and kinetics of NASICON NaxV2(PO4)3 cathode for sodium-ion batteries, Adv. Funct. Mater. 24 (27) (2014) 4265–4272.

[40] J. Gilmer, S.S. Schoenholz, P.F. Riley, O. Vinyals, G.E. Dahl, Neural message passing for quantum chemistry. International Conference on Machine Learning, PMLR, 2017, pp. 1263–1272.

[41] W. Hu, M. Shuaibi, A. Das, S. Goyal, A. Sriram, J. Leskovec, D. Parikh, C.L. Zitnick, et al., ForceNet: a graph neural network for large-scale quantum calculations, arXiv:2103.01436 [cs] (2021).

[42] J. Klicpera, F. Becker, S. Günnemann, GemNet: universal directional graph neural networks for molecules, in: A. Beygelzimer, Y. Dauphin, P. Liang, J.W. Vaughan (Eds.), Advances in Neural Information Processing Systems, 2021.https://openreview.net/forum?id=HS_sOaxS9K-

[43] B. Batzner, A. Musaelian, L. Sun, M. Geiger, J.P. Mailoa, M. Kornbluth, N. Molinari, T.E. Smidt, B. Kozinsky, E (3)-equivariant graph neural networks for data-efficient and accurate interatomic potentials, Nat. Commun. 13 (1) (2022) 2453.Nature Publishing Group UK London

[44] B.K. Miller, M. Geiger, T.E. Smidt, F. Noé, et al., Relevance of rotationally equivariant convolutions for predicting molecular properties, arXiv:2008.08461 [physics, stat](2020).

[45] T.S. Cohen, T.S. Cohen, U. Nl, Group equivariant convolutional networks. 33rd International Conference on Machine Learning, 2016, p. 10.

[46] R. Kondor, Z. Lin, S. Trivedi, Clebsch–Gordan Nets: a fully Fourier space spherical convolutional neural network. Advances in Neural Information Processing Systems volume 31, Curran Associates, Inc., 2018.

[47] N. Thomas, T. Smidt, S. Kearnes, L. Yang, L. Li, K. Kohlhoff, P. Riley, Tensor field networks: rotation- and translation-equivariant neural networks for 3D point clouds, 2018, 1802.08219.

[48] B. Anderson, T.S. Hy, R. Kondor, Cormorant: covariant molecular neural networks, in: H. Wallach, H. Larochelle, A. Beygelzimer, F.d. l. Alché-Buc, E. Fox, R. Garnett (Eds.), Advances in Neural Information Processing Systems vol. 32, Curran Associates, Inc., 2019.https://www.proceedings.neurips.cc/paper/2019/file/03573b32b2746e6e8ca98b9123f2249b-Paper.pdf

[49] Z. Qiao, A.S. Christensen, M. Welborn, F.R. Manby, A. Anandkumar, T.F. Miller III, UNiTE: unitary n-body tensor equivariant network with applications to quantum chemistry, arXiv:2105.14655 [physics](2021).

[50] Z. Deng, T.P. Mishra, E. Mahayoni, Q. Ma, A.J.K. Tieu, O. Guillon, J.-N. Chotard, V. Seznec, A.K. Cheetham, C. Masquelier, et al., Fundamental investigations on the sodium-ion transport properties of mixed polyanion solid-state battery electrolytes, Nat. Commun. 13 (1) (2022) 4470.

[51] T. Lombardo, M. Duquesnoy, H. El-Bouysidy, F. Årén, A. Gallo-Bueno, P. B. Jørgensen, A. Bhowmik, A. Demortière, E. Ayerbe, F. Alcaide, et al., Artificial intelligence applied to battery research: hype or reality? Chem. Rev. 122 (12) (2021) 10899–10969.

[52] J.H. Chang, P.B. Jørgensen, S. Loftager, A. Bhowmik, J.M.G. Lastra, T. Vegge, On-the-fly assessment of diffusion barriers of disordered transition metal oxyfluorides using local descriptors, Electrochim. Acta 388 (2021) 138551.

[53] J. Busk, P.B. Jørgensen, A. Bhowmik, M.N. Schmidt, O. Winther, T. Vegge, Calibrated uncertainty for molecular property prediction using ensembles of message passing neural networks, Mach. Learn. Sci. Technol. 3 (1) (2021) 015012.

[54] X. Fu, Z. Wu, W. Wang, T. Xie, S. Keten, R. Gomez-Bombarelli, T. Jaakkola, Forces are not enough: Benchmark and critical evaluation for machine learning force fields with molecular simulations, arXiv preprint arXiv:2210.07237(2022).

[55] D.P. Kingma, J. Ba, Adam: a method for stochastic optimization, arXiv preprint arXiv:1412.6980(2014).

[56] P.B. Jorgensen, A. Bhowmik, DeepDFT: neural message passing network for accurate charge density prediction, 2020, 2011.03346.

[57] P.B. Jørgensen, A. Bhowmik, Equivariant graph neural networks for fast electron density estimation of molecules, liquids, and solids, npj Comput. Mater. 8 (1) (2022) 1–10, https://doi.org/10.1038/s41524-022-00863-y.

[58] A. Musaelian, S. Batzner, A. Johansson, L. Sun, C.J. Owen, M. Kornbluth, B. Kozinsky, Learning local equivariant representations for large-scale atomistic dynamics, Nat. Commun. 14 (1) (2023) 579.

[59] V. Botu, R. Ramprasad, Adaptive machine learning framework to accelerate ab initio molecular dynamics, Int. J. Quantum. Chem. 115 (16) (2015) 1074–1083.

[60] E.V. Podryabinkin, A.V. Shapeev, Active learning of linearly parametrized interatomic potentials, Comput. Mater. Sci 140 (2017) 171–180.

[61] I.I. Novoselov, A.V. Yanilkin, A.V. Shapeev, E.V. Podryabinkin, Moment tensor potentials as a promising tool to study diffusion processes, Comput. Mater. Sci 164 (2019) 46–56.

[62] G. Sivaraman, A.N. Krishnamoorthy, M. Baur, C. Holm, M. Stan, G. Csányi, C. Benmore, A. Vázquez-Mayagoitia, Machine-learned interatomic potentials by active learning: amorphous and liquid hafnium dioxide, npj Comput. Mater. 6 (1) (2020) 104.

[63] X. Yang, A. Bhowmik, T. Vegge, H.A. Hansen, Neural network potentials for accelerated metadynamics of oxygen reduction kinetics at Au–water interfaces, Chem. Sci. 14 (14) (2023) 3913–3922.

[64] L. Zhang, J. Han, H. Wang, R. Car, E. Weinan, Deep potential molecular dynamics: a scalable model with the accuracy of quantum mechanics, Phys. Rev. Lett. 120 (14) (2018) 143001.

[65] M. Burbano, D. Carlier, F. Boucher, B.J. Morgan, M. Salanne, Sparse cyclic excitations explain the low ionic conductivity of stoichiometric Li7La3Zr2O12, Phys. Rev. Lett. 116 (13) (2016) 135901.

[66] G. James, D. Witten, T. Hastie, R. Tibshirani, An introduction to statistical learning vol. 112, Springer, 2013.

[67] Y. Ishado, A. Inoishi, S. Okada, Exploring factors limiting three-na+ extraction from Na3V2(PO4)3, Electrochemistry (2020) 20–00080.

[68] G. Henkelman, A. Arnaldsson, H. Jónsson, A fast and robust algorithm for Bader decomposition of charge density, Comput. Mater. Sci 36 (3) (2006) 354–360.

[69] H. Jónsson, G. Mills, K.W. Jacobsen, Nudged elastic band method for finding minimum energy paths of transitions (1998).

[70] N.J.J. de Klerk, E. van der Maas, M. Wagemaker, Analysis of diffusion in solid-state electrolytes through MD simulations, improvement of the li-ion conductivity in β-li3PS4 as an example, ACS Appl. Energy Mater. 1 (7) (2018) 3230–3242.

[71] X. He, Y. Zhu, Y. Mo, Origin of fast ion diffusion in super-ionic conductors, Nat. Commun. 8 (1) (2017) 15893.

[72] P. Banerjee, S. Yashonath, B. Bagchi, Rotation driven translational diffusion of polyatomic ions in water: a novel mechanism for breakdown of stokes-einstein relation, J. Chem. Phys. 146 (16) (2017) 164502.

[73] D. Siegel, Charge transport in lithium peroxide: relevance for rechargeable metal-air batteries. 2014-Sustainable Industrial Processing Summit vol. 4, Flogen Star Outreach, 2014, pp. 387–388.

[74] S.P. Ong, Y. Mo, G. Ceder, Low hole polaron migration barrier in lithium peroxide, Phys. Rev. B 85 (8) (2012) 081105.

[75] T.L. Tran, H.D. Luong, D.M. Duong, N.T. Dinh, V.A. Dinh, Hybrid functional study on small polaron formation and ion diffusion in the cathode material Na2Mn3 (SO4)4, ACS Omega 5 (10) (2020) 5429–5435.